VNIVERSITAT DE VALÈNCIA Facultat de Física

Treball de fi de Grau en Física

Models estacionaris de dolls extragalàctics

Juliol de 2017

Alumne: Andreu Anglés Castillo

Tutor (1): José María Martí Puig
Tutor (2): Manel Perucho Pla

Contents

Abstract

The present work has as an object of study extragalactic jets. These jets are generated through the extraction of rotation energy of the black hole in the center of some active galaxies. The radiation presented by these objects is the synchrotron radiation. To do this study stationary and axialsymmetric jets are modelled to simplify the system of equations that governs the system. We have simulated this model in a numerical simulation program and modified it to simulate different ambient medium conditions that affect the shape and behaviour of the jet. In particular, this study ends with the simulation of an ambient medium which mass loads the jet decelerating it. In the astronomical context this characteristic is presented by Fanaroff-Riley I active galaxies.

Abstract

El present treball té com a objecte d'estudi dolls extragalàctics. Aquests dolls es generen mitjançant l'extracció d'energia de rotació del forat negre al centre de certes galàxies actives. La radiació que presenten aquests objectes està dominada per la radiació sincrotró. Per a realitzar l'estudi es modelen jets estacionaris i amb simetria axial per tal de simplicar el sistema d'equacions que governa el sistema. Hem simulat el model en un programa de simulació numèrica i l'hem modificat per a simular diferents condicions ambientals que afecten enormement la forma i comportament del jet. En particular, l'estudi culmina amb la simulació d'una atmòsfera que carrega de massa el jet desaccelerant-lo. En l'àmbit astronòmic aquesta característica la presenten les galaxies actives classificades com Fanaroff-Riley I.

1 Introduction

We are going to focus our study on the plasma dynamics of jets originated in the center of Active Galaxy Nuclei (AGN), which are the central part of active galaxies. These galaxies present the highest luminosities in the sky in a large portion of the electromagnetic spectrum. An AGN is a galaxy that emits light outside the spectrum spected by the emission of light coming from stars, indicating that it does not come from nuclear reactions in stars but from some other mechanisms. The main source of emission of light is the synchrotron radiation, which is the radiation emitted when charged particles with relativistic velocities are accelerated by a magnetic field. The AGNs that we are going to focus on are the one with radioloud emission, i.e. the ones whose power is the highest in the radio spectrum. These AGN are composed by a super-massive black hole (SMBH), on the order of millions to thousands of millions of solar masses, an accretion disk around the black hole, a ring of stellar dust around the nucleus and two jets emerging in opposite directions. In Fig. 1 a schematic picture of an AGN is shown. These radio galaxies are classified into two categories as introduced by Fanaroff and Riley (FR) in [1]. Depending on their luminosity in the radio spectrum and its distribution they are classified into FRI or FRII. On the one hand, FRI active galaxies have a high luminosity nucleus and the parts of the jets in regions close to the AGN only, and do not present any lobe far away from the nucleus. On the other hand, FRII galaxies have a luminous nucleus but low luminosity jets and high luminosity lobes, which are formed at the end of the jets and are distant from the AGN. In Fig. 2 we show a comparison between these two types of AGN. The properties of FRI jets suggest that they are subject to some kind of deceleration, for example, caused by mass loading by stellar winds, which is the ultimate study point of this work. Another mechanism proposed in the literature to explain the disruption of FR I jets is the growth of instabilities, but given the nature of our work we are not able to explore that option.

Relativistic jets are flows of charged particles that have velocities close to the speed of light. Usually, charged particles referred to as plasma, can be a mixture of ions and free electrons. These particles tend to arrange themselves to acquire an overall charge neutrality, the particles responsible for this are usually the electrons (or positrons) being much lighter than ions hence having more mobility. What mainly differentiates the behaviour of plasmas from that of a neutral gas or liquid is that plasmas are subject to long range interacting forces, namely electromagnetic forces. If some requirements are met, the macroscopic description of plasmas can be made through the magnetic field created by the motion of charges which, at the same time, dictates the dynamics of plasma. To complete the description of plasma dynamics, relativistic effects must be taken into account if the plasma has flow velocities close to the speed of light. The theory that describes these plasma dynamics is called magneto-hydrodynamics (MHD).

The jet formation is a very complicated process and requires a deep study of dynamics around the SMBH including general relativistic effects. Even though the formation process of the jet is out of the scope of this work we give a qualitative description following Chapter 4 of [2] to have a bigger picture of what relativistic jets are. First of all we consider that the SMBH is surrounded by an atmosphere of plasma (or magnetosphere), created by the accretion of plasma particles with a magnetic field associated and carried with them. The accretion disk and the magnetosphere are orbiting the black hole (BH) so that this movement of charged particles creates a poloidal magnetic field B_p. We start assuming that magnetic field lines go out through the north hemisphere of the BH and enter its

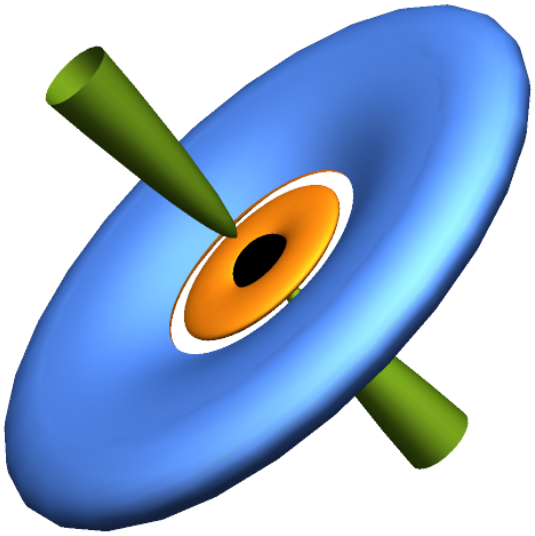

Figure 1: Schematic picture of an AGN. In black is represented the SMBH, in orange the accretion disk, in blue the stellar cloud and in green two jets emerging from the black hole.

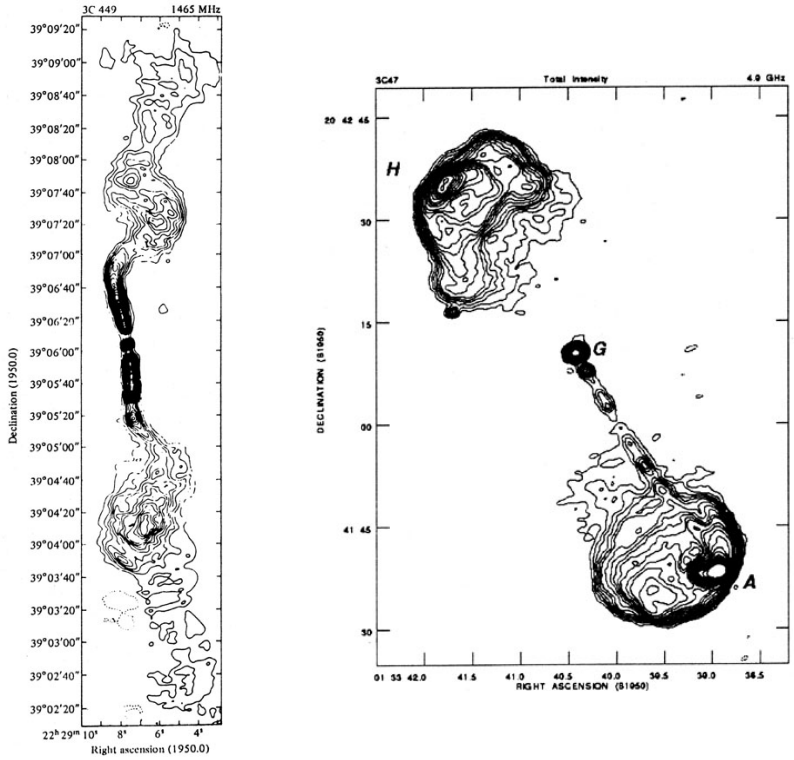

Figure 2: Two examples showing the main differences in the Fanaroff- Ridley classification. On the left, we have an FRI AGN with a bright nucleous and jets that break down as they get away from the nucleus. On the right, a FRII galaxy presents a bright nucleus and hotspots and the end of the jets. We cannot see the jet that is moving away the observer caused by Doppler boosting (emission of electromagnetic radiation in the direction of propagation). Darker areas represent higher brightness. Images reproduced from Perley, Willis and Scott (1979) and Alan Bridle (1994), respectively.

south hemisphere. A schematic of this whole process is shown in Fig. 3. Now as the charged particles orbit through this magnetic field they will experience a Lorentz force $\mathbf{F} = q(\mathbf{E} + \mathbf{v} \times \mathbf{B})$ perpendicular to their motion and the magnetic field, so that positively charged particles will move towards the equator of the BH and negative ones to the poles. With this configuration we see that our initial hypothesis was correct as positive charges moving around the equator sustain the poloidal magnetic field. Now as the magnetosphere is made of free charges they will act as a conductive medium and a current will appear from the poles to the equator. This current will have two effects, a force opposing the rotation motion of the black hole (extraction of rotational energy of the BH) and the appearance of a toroidal magnetic field B_ϕ in the opposite direction of the BH rotation through Ampère's law

$$\nabla \times \mathbf{B} = \mathbf{J} \ , \tag{1}$$

where $\mathbf{J}$ is the current. In MHD the magnetic fields have two dynamical contributions, the magnetic pressure, which we shall introduce later, and magnetic tension. The magnetic tension is a force that appears in curved field lines and is directed along their curvature radius and depends inversely on its modulus. This will cause an extreme force directed towards the center of curvature of the field lines and, as there is material in between, this will result in a high pressure and, as plasma particles are constrained to move around field lines, they will get accelerated outwards if that pressure can overcome the gravitational potencial of the BH. The magnetic field configuration on the emerging jet is an helical one and can be characterized by a pitch angle. This angle will not be the same as the jet evolves due to a phenomenon known as magnetic flux freezing. Flux freezing is when magnetic field-lines appear to get carried along with the flow of a perfectly conducting fluid, this translates to: the magnetic flux through any closed contour in the fluid does not change, no matter how complex the evolution of the contour is. This will have as a consequence that the magnetic field will decrease as the jet expands. The poloidal magnetic field-lines are perpendicular to the cross-section of the jet which area increases $\propto r^2$ and to keep the magnetic flux constant the poloidal field strength will decrease. Meanwhile, the area perpendicular to toroidal field lines escalates $\propto r$ meaning that the poloidal magnetic field will decrease more than the toroidal magnetic field during the jet expansion.

As the jet gets away from the AGN it gets accelerated and gravitational effects are negligible. This regime is where we are going to focus our work. To describe the jet in this scenario we are going to make use of the equations of MHD, which describe magnetic field dynamics and fluid dynamics as a whole. This study is done in detail in the next section.

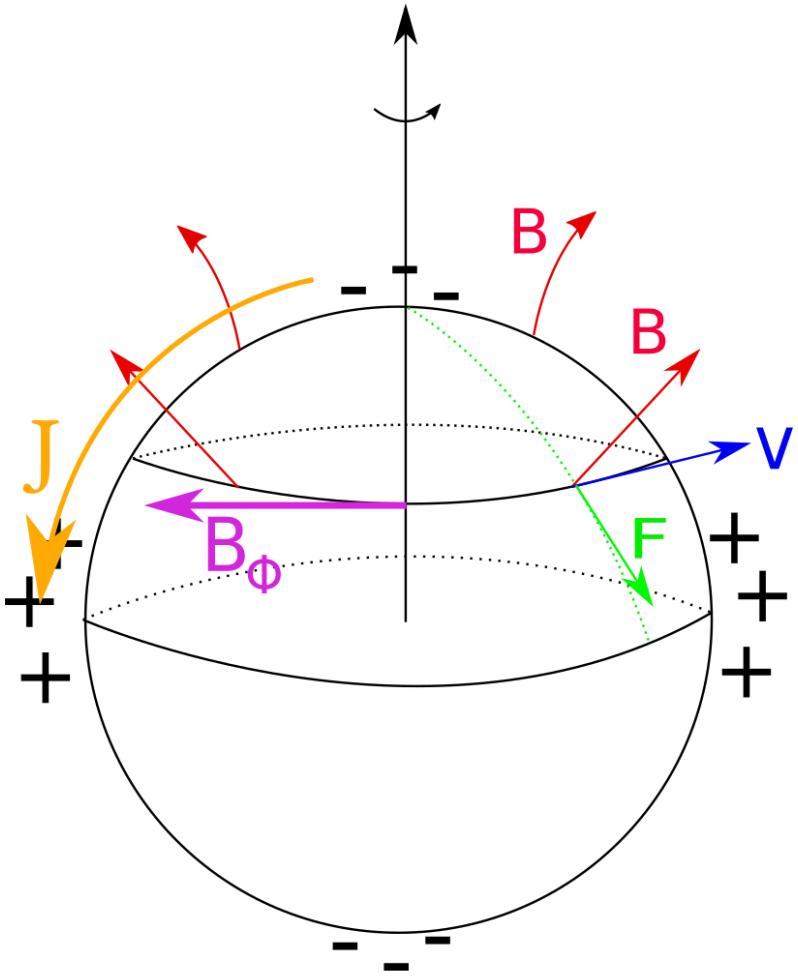

Figure 3: Schema of the magnetic field configuration. We have a poloidal magnetic field (red lines) and a flow of charged particles (blue arrow) which generate a force directed along the green arrow for positives charges and in the opposite direction for negatives ones. This creates a configuration where positives particles are gathered around the equator and negatively charged particles are displaced to the poles. As the atmosphere is a perfect conductor this configuration creates a current (orange line) which has two effects. On the one hand, together with the poloidal magnetic field (red arrows) creates a Lorentz force opposing the rotation of the BH. On the other hand, through Eq. 1 creates a toroidal magnetic field represented by the purple arrow.

2 Model and approximations

MHD equations are the set of equations governing fluid dynamics, i.e. continuity equations and conservation of energy-momentum tensor along with an equation of state (EoS), which by themselves are a complicated set of coupled equations that do not have analytic solution and numerical methods have to be applied. Then we have Maxwell's equations describing field dynamics and finally the Ohm's law for ideal MHD. So far, these equations pose an intractable problem. To make it tractable at a graduate student level we are going to consider axially symmetric, steady state jet models. Hence, with the use of cylindrical coordinates, the variables defining the jet will depend only on the z direction, the symmetry axis, and the r coordinate, meaning that all partial derivatives with respect to time and the polar coordinate will vanish. In addition to this, our magnetohydrodynamical models have been computed following the approach developed by [3] that allows to study the structure of steady, axisymmetric relativistic (magnetized) flows using one-dimensional time-dependent simulations. The approach is based on the fact that for narrow jets (*quasi-one-dimensional approach*) with axial velocities close to the speed of light the steady-state equations of relativistic magnetohydrodynamics can be accurately approximated by the one-dimensional time-dependent equations with the axial coordinate acting as the *temporal* coordinate.

2.1 Relativistic Magnetohydrodynamical equations

Now, we proceed presenting the equations of relativistic magnetohydrodynamics and the simplifications leading to the actual set of equations used in the present work[1]. We start with conservation laws, first the equation of continuity which states conservation of mass and reads

$$\partial_t \rho\Gamma + \nabla \cdot (\rho\Gamma\mathbf{v}) = 0 \ , \tag{2}$$

where ρ is the plasma density, $\Gamma = 1/\sqrt{1-v^2}$ the usual Lorentz factor and $\mathbf{v}$ the flow velocity. The energy and momentum conservation is expressed by the conservation of the energy-momentum tensor:

$$\nabla_\mu T^{\mu\nu} = \partial_t T^{t\nu} + \nabla_j T^{j\nu} = 0 \ , \tag{3}$$

where ∇_j represents the divergence in cylindrical coordinates and $T^{\mu\nu}$ the energy-momentum tensor which has two contributions, one hydrodynamical and the other electromagnetic. The energy-momentum tensor reads

$$T^{\mu\nu} = h\rho u^\mu u^\nu + p_t g^{\mu\nu} - b^\mu b^\nu \ , \tag{4}$$

with $g^{\mu\nu}$ the Minkowski metric, h the hydromagnetic enthalpy, p_t the total pressure, $u^\mu = \Gamma(c, \mathbf{v})$ the four velocity and $b^\mu = (b^0, \mathbf{b})$ the magnetic field four-vector in the fluid rest-frame with components:

$$b^0 = \Gamma(\mathbf{v} \cdot \mathbf{B}) \ , \tag{5}$$

$$\mathbf{b} = \frac{\mathbf{B}}{\Gamma} + b^0\mathbf{v} \ , \tag{6}$$

[1]Along this section, we use the summation convention on repeated indices with Latin ones running from 1 to 3 and Greek ones from 0 to 3. Besides that we use units in which the speed of light is set to 1, and absorb the 4π factor in the definition of the magnetic field.

where **B** is the magnetic field. Note that we introduced a total pressure because it has two components, a pressure associated with the fluid and a magnetic pressure, i.e.,

$$p_t = p + p_{\rm mag} = p + \frac{b_\mu b^\mu}{2} \ . \tag{7}$$

This magnetic contribution to the pressure in the momentum equation comes from the Lorentz force. The other contribution of this force is through a term of magnetic tension. The hydromagnetic enthalpy is

$$h = 1 + \epsilon + \frac{p}{\rho} + \frac{b_\mu b^\mu}{\rho} \ , \tag{8}$$

where ϵ is the specific internal energy and p, ρ and ϵ are related by the following ideal-gas equation of state:

$$p = (\gamma - 1)\rho\epsilon \ , \tag{9}$$

where γ is the adiabatic index. We finally introduce the equations that govern the electromagnetic field, these are the homogeneous Maxwell's equations,

$$\partial_t \mathbf{B} + \nabla \times \mathbf{E} = 0 \quad \text{(Faraday's equation)}, \tag{10}$$

$$\nabla \cdot \mathbf{B} = 0 \quad \text{(Divergence free constrain)}, \tag{11}$$

and the ideal MHD Ohm's law

$$\mathbf{E} = -\mathbf{v} \times \mathbf{B} \ , \tag{12}$$

where **E** is the electric field .

2.2 Quasi one-dimensional approximation

We are now able to present the approximations [3] that will simplify this system of equations. First, let us remind that our models are stationary and axisymmetric (i.e., the terms involving time derivatives and angular derivatives are dropped).

1.First Approximation: $z \gg r$**.** We are focusing on the study of narrow jets and the condition of $z \gg r$ encapsulates this condition, actually the simulations we run have radius of the order of a parsec and a longitude of hundreds to thousands of parsecs. For simple enough configurations this condition naturally leads to models with

$$v^r \ll v^z, \tag{13}$$

$$B^r \ll B^z. \tag{14}$$

Concerning this last expression, consistency with the one-dimensional version of the divergence free condition forces to consider configurations with very small radial components of the magnetic field ($B^r \ll \max(B^\phi, B^z)$).

2. Second Approximation: $v^z \approx c$**.** This implicitly means that $v^r \ll v^z$ (consistently with the first approximation) and $v^\phi \ll v^z$.

All these constraints should be verified *a posteriori*, once the approximate two-dimensional solution has been obtained.

2.3 The final equations

With these approximations, the axisymmetric, time-independent system of equations reduces to a 1D system of the form:

$$\partial_t U(t,r) + \nabla_r F(t,r) = S(t,r) \ , \tag{15}$$

where ∇_r represents the derivation with respect to r in the context of cylindrical coordinates, i.e. $\nabla_r f(t,r) = \frac{1}{r}\partial_r(rf(t,r))$. We will explain in the next section the remaining symbols in this equation.

Continuity equation. Simply by applying the conditions of steady-state and axisymmetry, where partial derivatives in time and polar coordinate vanish, Eq. 2 reduces to

$$\nabla_r(\rho\Gamma v^z) + \partial_z(\rho\Gamma v^z) = 0 \ . \tag{16}$$

Now making use of our convention to use the z coordinate as time we take $\partial_z \to \partial_t$ and the condition of ultra-relativistic jet in the axial direction makes $v^z = 1$ leading to

$$\partial_t(\rho\Gamma) + \nabla_r(\rho\Gamma v^z) = 0 \ , \tag{17}$$

which has the desired form of Eq. 15. Now we will proceed in a similar fashion for the rest of equations.

Faraday's equation. We will use the ideal MHD Ohm's law to reduce the Faraday equation to a equation for the dynamics of the magnetic field. As we showed earlier we will not have a a radial component of the magnetic field.

$$\left.\begin{array}{c} \mathbf{E} = -\mathbf{v}\times\mathbf{B} \implies \nabla\times\mathbf{E} = -\nabla\times(v\times\mathbf{B}) \\ \partial_t\mathbf{B} + \nabla\times\mathbf{E} = 0 \end{array}\right\} \implies \partial_t\mathbf{B} = \nabla\times(v\times\mathbf{B})$$

- *ϕ component of the magnetic field.* Direct operations lead to

  $$\partial_t B^\phi = \partial_z(v^\phi B^z) - \partial_z(v^z B^\phi) - \partial_r(v^r B^\phi) + \partial_r(v^\phi B^r) \ .$$

  First we realize that the most significant terms are the second and the third in the RHS of the above equation. Making use of our approximation $B^r = 0$ and the steady-state condition and ignoring the least significant terms we can proceed as before to get:

  $$\partial_t B^\phi + \partial_r(v^r B^\phi) = 0 \implies \partial_t B^\phi + \frac{1}{r}\partial_r(r v^r B^\phi) = \frac{v^r B^\phi}{r} \ , \tag{18}$$

  where integration by parts was done to recover an equation in the form of Eq. 15.

- *z component of the magnetic field.* Here a similar procedure is followed to obtain:

  $$\partial_t B^z + \nabla_r(v^r B^z) = 0 \ . \tag{19}$$

Conservation of the energy-momentum tensor. The computation of all the individual components of the energy-momentum tensor conservation are long and straightforward calculations so that we give the final results:

$$\partial_t(\rho h\Gamma^2 v^r - b^0 b^r) + \nabla_r(\rho h\Gamma^2 (v^r)^2 + p_t - (b^r)^2) = \frac{p_t - (b^\phi)^2}{r} \ ; \tag{20}$$

$$\partial_t(\rho h\Gamma^2 - b^0 b^z) + \nabla_r(\rho h\Gamma^2 v^r - b^r b^z) = 0 \ ; \tag{21}$$

$$\partial_t(-b^0 b^\phi) + \nabla_r(-b^\phi b^r) = \frac{b^\phi b^r}{r} \ ; \tag{22}$$

$$\partial_t(\rho h\Gamma^2 - p_t - (b^o)^2 - \rho\Gamma) + \nabla_r(\rho h\Gamma^2 v^r - b^r b^0 - \rho\Gamma) = 0 \ , \tag{23}$$

where $b^0 = \Gamma B^z$, $b^r = \Gamma v^r B^z$, $b^\phi = B^\phi/\Gamma$ and $b^z = \frac{\Gamma^2+1}{\Gamma} B^z$.

3 Simulation

3.1 Numerical code

As noted in the previous section, the set of equations (17)-(23) are all of the form

$$\partial_t U(t,r) + \nabla_r F(t,r) = S(t,r) \ . \tag{24}$$

As the more general RMHD system of equations, this set of non-linear, partial differential equations forms a hyperbolic system of conservation laws (see, e.g., [4]), where U represents a conserved quantity, F is its corresponding flux, and S a source term.

In a hyperbolic system, if the solution is known in some spatial domain at some given time, the hyperbolicity of the equations can be used to advance the solution to some later time (initial value problem). In general, it is not possible, however, to derive an exact solution. Instead one has to rely on numerical methods which provide an approximate solution. Moreover, the numerical methods must be able to handle solutions with discontinuities (i.e., shocks), which are inherent to non-linear hyperbolic systems.

Among the numerical methods devised to solve this kind of equations are the so-called *high-resolution shock-capturing* (HRSC) methods that solve a discretized version of the system keeping its conservation form. HRSC methods are time-marching procedures in which the hyperbolic equation is solved on a discrete space-time numerical grid (r_i, t^n) with

$$r_i = (i - 1/2)\Delta r, \quad i = 1, 2, \dots \ , \tag{25}$$

and

$$t^n = n\Delta t, \quad n = 0, 1, 2, \dots \tag{26}$$

(where Δt and Δr are the time step and the cell size, respectively), aiming to obtain an approximation of the solution at $r = r_i$, $t = t^n$, U_i^n, from the known approximations of previous time steps according to the following scheme (first-order in time and adapted to cylindrical radial geometry)

$$U_i^{n+1} = U_i^n - \frac{\Delta t}{\Delta r}\left(r_{i+1/2}\hat{F}_{i+1/2} - r_{i-1/2}\hat{F}_{i-1/2}\right) + \Delta t S_i^n. \tag{27}$$

In the previous expression, S_i^n is an approximation to the value of the source term at $r = r_i$, $t = t^n$, and $\hat{F}_{i+1/2}$ is an approximation to the average flux F through the interface between numerical zones $r = r_i$ and $r = r_{i+1}$ along the time step between $t = t^n$ and $t = t^{n+1}$.

HRSC schemes proceed along the main steps: i) *zone reconstruction*: in order improve the quality of the solution without increasing the number of computational zones, the solution inside them is interpolated with appropriate zone-reconstruction algorithms; ii) *computation of numerical fluxes*: using the interpolated values of the solution at both sides of an interface, the numerical fluxes between zones are computed by means of sophisticated algorithms to account for the hypothetical development of shocks (discontinuities in the solution), iii) *time advance*: high-order algorithms are used to advance in time the solution with high precision.

Having advanced the conserved variables in time, primitive variables (rest-mass density, pressure, flow velocity components, magnetic field components) have to be recovered after each time step since they are needed to compute the numerical fluxes for the next time iteration. Finally, besides the solution at some initial time, boundary conditions at the borders of the computational grid should be provided along the simulation.

The one-dimensional simulations performed in this work have been done with an adapted version of a two-dimensional code developed by my supervisors in which I have implemented appropriate initial models and boundary conditions, as well as the source term representing the mass loading of jets.

3.2 Numerical grid and boundary conditions

Since we are interested in axisymetric, steady jet models, we use a (r, z) cylindrical grid where $0 < r < L_r$, and $0 < z < L_z$, where L_r and L_z, the maximum radial and axial grid lengths, respectively, depend on the type of simulation. The initial condition, with a relativistic jet entering the grid between $0 < r < R_j$ (R_j being the radius of the jet), is set at $z = 0$ (the jet base). Boundary conditions along the time should also be provided at the jet axis, $r = 0$, and at the jet surface (tracked with the help of a marker of the jet material). This jet surface tracer is a control variable whose values range from 1, where the jet is not mixed with ambient material, and 0, which represents material from the ambient, intermediate values represent mixtures of the jet original material and the medium's. The outer boundary at $r = L_r$ is irrelevant in the present calculations. The ambient medium between the outer boundary of the radial grid and the jet surface is characterized by its density and pressure (and the absence of velocity and magnetic field).

3.3 Model parameters

In this subsection we present the parameters that we fixed, and the ones derived from them, required to set the initial state of the jet. We begin by setting the power of the jet. As introduced in section 1 and pointed out in [5–7] FRI jets are thought to be subjected to a deceleration produced by mass entrainment of stellar winds and instabilities. As instabilities require a non-steady state model we can only deal with the phenomenon of mass entrainment. Following the study in [7] and the Fig. 1 in it, we restrict the jet power at $L_j = 10^{43}$ erg/s to ensure that we are working with a FRI type of jet. The power or energy flux of the jet has 3 contributions: the kinetic energy flux, internal energy flux and Poynting flux (electromagnetic energy flux). We fix the ambient medium pressure and density to physically reasonable values. As argued in section 2 we have to work with jets having high Lorentz factors, we decided to take $\Gamma = 5$, which corresponds to an axial velocity of $v_z = 0.98c$. We have chosen to study the behavior of jets with different dominance of the magnetic fields. This dominance is quantified by the magnetization parameter, which is the ratio between the magnetic pressure and hydrodynamic pressure, i.e. $\beta = p_m/p$. We have simulated jets with magnetizations $\beta = 0.1$, $\beta = 1$ and $\beta = 10$. We know that, in our model, the magnetic field has two components, the poloidal component is constant along the radius and has a smooth step at the border of the jet. We call the profile of variables at the border the shear layer, which is a smoothed step function. The toroidal component has a special boundary condition, it is null at the center of the jet, its profile along the radial direction increases quasi-linearly up to a maximum point and then monotonically decreases up to the border of the jet. We worked with jets that are in equilibrium with the ambient medium at injection, this is parameterized with the overpressure parameter, and in our case it is the unit. We have also simulated some jets with an overpressure parameter of $K = 2$ to unravel the shock structure that jets naturally present. With these fixed parameters we can derive the remaining parameters of interest. With the values of external pressure, magnetization and Lorentz factor, together

with the pressure equilibrium condition (depending on K) between the ambient medium and the jet, we can derive the pressure of the jet for different values of β. The density of the jet is set equal to the density of the ambient medium. Making use of the equation of state we can now calculate the internal energy of the jet, where we have set the adiabatic index to $\gamma = 4/3$ which corresponds to a thermally relativistic gas. With that we can calculate the different contributions to the power of the jet and with our fixed value for FRI jets derive the jet radius for different magnetizations. Finally, with these parameters, the characteristic values for the magnetic field components are obtained.

Our study will start by inspecting jets in a homogeneous ambient medium, which is characterized by a constant pressure and density over space. The density is set to be equal to the jet's one, and the pressure is a fixed parameter. Then we move to simulations of jets in a more realistic atmosphere and give the pressure a decaying profile characterized by the value of r_C, which is the host galaxy core radius. Finally, to account for the deceleration of jets, a source term q is added in the calculations to the continuity equation (Eq. 2) with a tracer value of 0, which will also have a dependence on the distance from the galaxy in the same fashion as the external pressure, as well as a density profile, with q_0 the mass entrainment rate at the center of the host galaxy. In Table 1 we gather some of the parameters mentioned above and give names to the models we have simulated. Simulations inject the initial parameters at 10 pc from the BH.

Model	R_j[pc]	β	r_C[pc]	$q_0[\rho_0 c/\text{pc}]$	K	$\epsilon_j[c^2]$
Jo11	1	0.1	N/A	0	1	1.8
Jo12	1	1	N/A	0	1	1.0
Jo13	1	10	N/A	0	1	0.2
Jo21	1	0.1	N/A	0	2	1.8
Jo22	1	1	N/A	0	2	1.0
Jo23	1	10	N/A	0	2	0.2
Jp21	1	0.1	20	0	1	1.8
Jp22	1	1	20	0	1	1.0
Jp23	1	10	20	0	1	0.2
Jp51	1	0.1	50	0	1	1.8
Jp52	1	1	50	0	1	1.0
Jp53	1	10	50	0	1	0.2
Jm01	1.7	0.1	250	9.2×10^{-7}	1	1.8
Jm02	2.0	1	250	9.2×10^{-7}	1	1.0
Jm03	2.8	10	250	9.2×10^{-7}	1	0.2
Jm11	1.7	0.1	250	9.2×10^{-6}	1	1.8
Jm12	2.0	1	250	9.2×10^{-6}	1	1.0
Jm13	2.8	10	250	9.2×10^{-6}	1	0.2
Jm21	1.7	0.1	250	9.2×10^{-5}	1	1.8
Jm22	2.0	1	250	9.2×10^{-5}	1	1.0
Jm23	2.8	10	250	9.2×10^{-5}	1	0.2
Jm30	2.8	1	250	0	1	0.2

Table 1: Models names and parameters. Here $\rho_0 = 10^{-26} g/cm^3$.

4 Results

4.1 Homogeneous ambient medium

These are the series of models with the prefix "Jo" and represent the basic simulation models as there is not much evolution in the shape of the jets. We present these models to explain the many outputs of our simulation and check that the approximations we made within the MHD equations are still correct. Figure 5 shows the model Jo12 with 6 panels representing the contour plots of some variables of interest up to a longitude corresponding to 200 radii of the jet. The first panel shows the contour of the density, it can be readily seen that the shape of the jets does not change along it. The tracer plotted in this panel shows contours corresponding to 0.05 and 0.95, the outer one corresponding to the value 0.05 shows that there is no mixing at all with the ambient medium. This panel also shows a faint structure of shocks caused by a fine detuning of the overpressure parameter. We leave an interpretation of the second panel for later. The third panel shows the toroidal velocity field where the light green color outside and inside the jet represents no rotation velocity and there is a small velocity in the border of the jet due to the diffusion of the shear layer. As can be seen from the color scale on the right of this panel, this velocity does not get close to relativistic showing that our 2nd approximation in section 2 holds. The following panel represents the Lorentz factor which stays constant along the whole jet. The last two panels represent the toroidal and poloidal components of the magnetic field respectively with no evolution at all, as expected. We can see the toroidal magnetic field profile described before, where it is null in the center arrives to some maximum and then monotonously decreases to the edge. We now proceed to interpret the second panel, which shows the hydrostatic pressure. As explained before there are two contributions to the pressure, the magnetic and the hydrostatic. In the figure we see that hydrostatic pressure is higher in the center of jet and lower in the region closer to the border coinciding with the maximum of the toroidal magnetic field. The total pressure is in equilibrium with the medium outside and constant, a slice of these two contributions at a constant distance from the injection point is shown in Fig. 4a. We see that the total pressure inside and outside the jet coincide on the border of the jet and that outside, where there is no magnetic field, the total pressure and the hydrostatic pressure coincide. In Fig. 4b we compare the magnetic pressure between the models Jo11, Jo12 and Jo13 which present different magnetizations ($\beta = 0.1, 1, 10$ respectively).

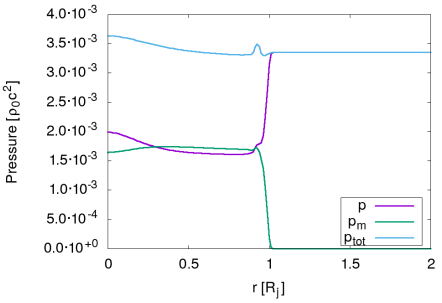

(a) Magnetic and hydrostatic pressure profiles for the Jo12 model, which has a maneti-zation parameter $\beta = 1$.

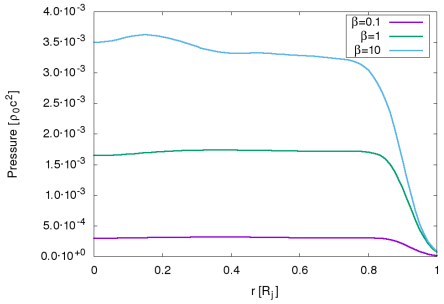

(b) Comparison of the magnetic pressure for different magnetizations, namely models Jo11, Jo12 and Jo13.

Figure 4: Comparisons of different contributions to the pressure.

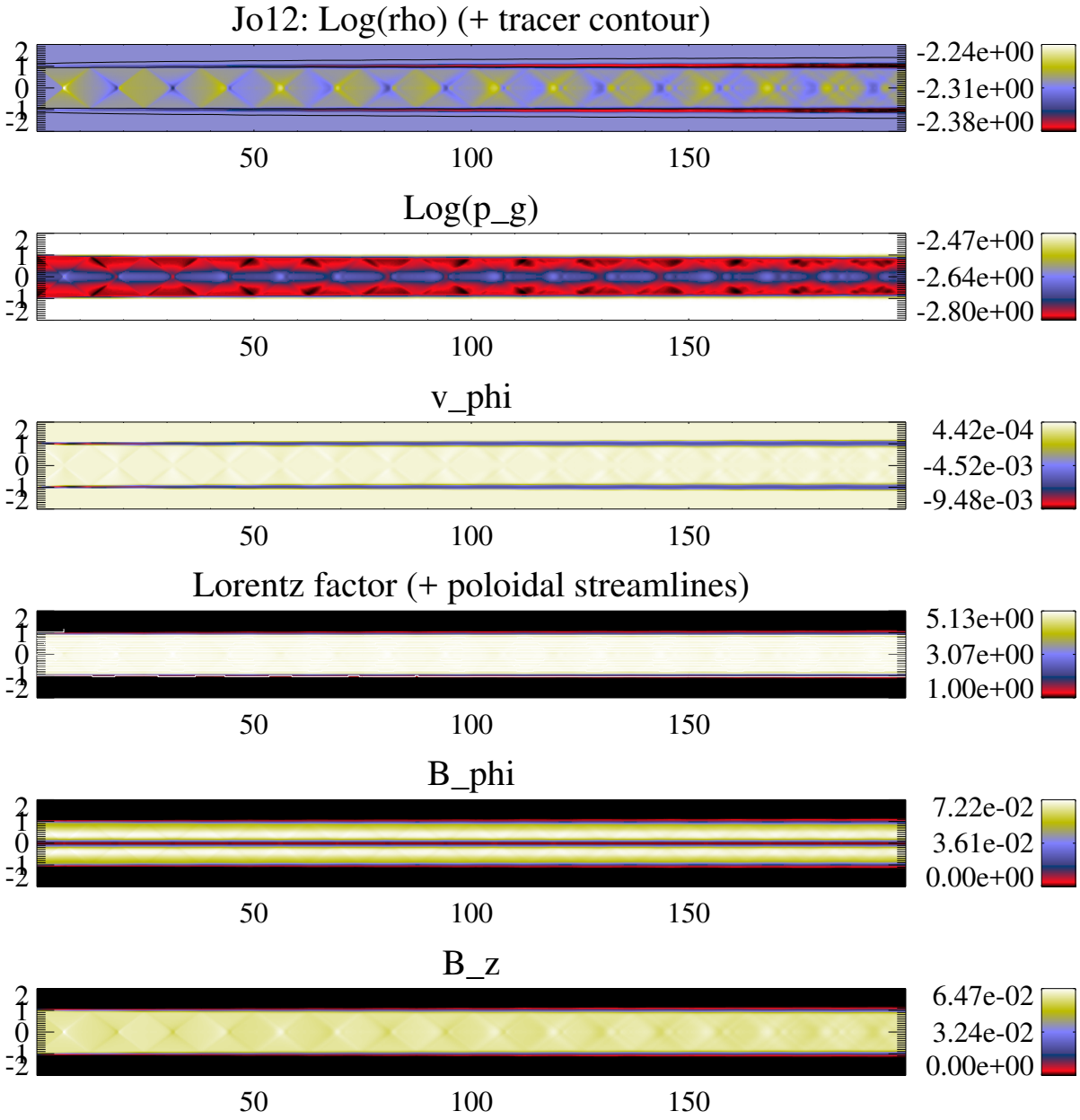

Figure 5: Model of a jet with $\beta = 1$ with an overpressure parameter $K = 1$ in a homogeneous atmosphere. Variables are expressed in units of the jet radius, R_j, the speed of light, c, and the fiducial density ρ_0.

4.1.1 Overpressured jet

To unravel the shock structure that is formed when there is a difference on the conditions of the ambient medium and the jet we change the overpressure parameter of the previous simulations and show the model Jo22 in Fig. 7. We are still infront of a model that does not show evolution over time, but a pattern repeated over and over. Being in a situation where there is no equilibrium with the ambient medium, the shape of the jet changes. In this case, the jet first expands as it is more pressured than the ambient medium, then it exceeds the equilibrium state and the ambient medium has more pressure than the jet, creating a back and forth movement, that keeps on going indefinitelly. These shocks come with an increase (decrease) of some jet parameters when the jet is compressed (expanded), for instance, density, pressure and magnetic field. Note that the Lorentz presents the opposite behaviour, it increases when the jet presents the bigger appertures, effect that we will study in depth in the next section.

In Fig. 6 we compare the shock structure for models with different magnetizations, we see that the model with less magnetization presents less shocks than models with more magnetization over the same distances. This effect is produced by the magnetic tension, a force that we introduced in section 1 and opposes the jet expansion, which has a bigger impact on jets with larger magnetizations. This makes more magnetized jets to have a faster compression after the expansion initially caused by the overpressure, with respect to less magnetized jets.

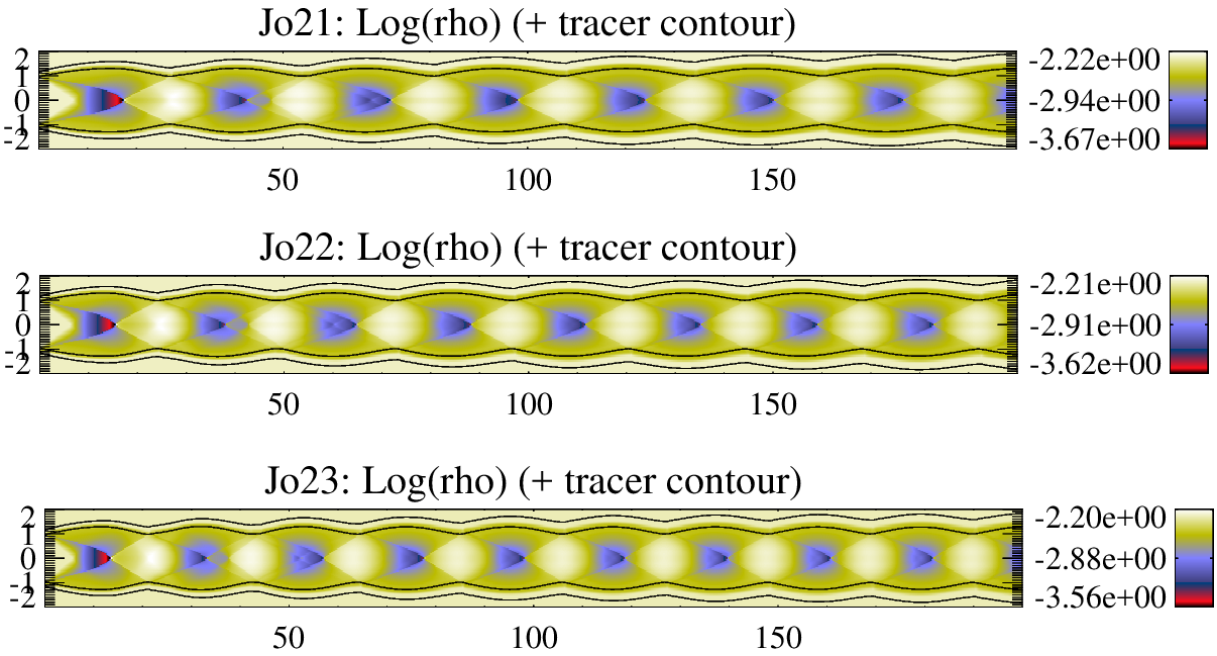

Figure 6: Comparison of the shock structure for models with different magnetizations and overpressure parameter $K = 2$. From top to bottom are plotted the density panels of the models Jo21, Jo22 and Jo23, respectively. Model Jo21 presents 8 recollimation shocks, Jo22 nearly 9 of these shocks and Jo23 presents 10.

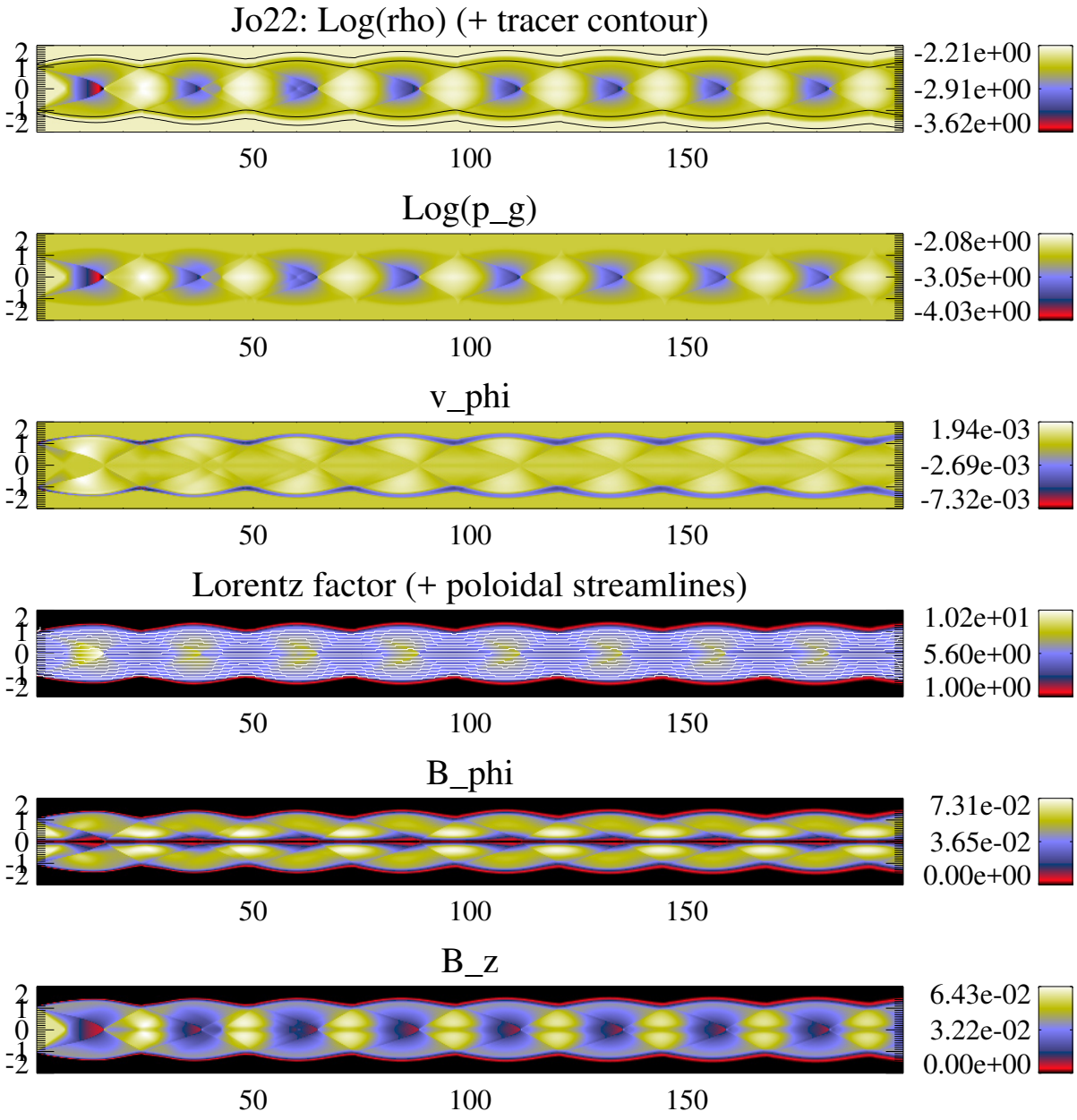

Figure 7: Model of a jet with $\beta = 1$ with an overpressure parameter $K = 2$ in a homogeneous atmosphere.

4.2 Ambient medium with a pressure profile

Now that we have a general picture on how to interpret jet parameters we move to a more realistic scenario having a decaying pressure in the ambient medium. The profile we programmed for the ambient pressure is [5, 8]

$$p(z) = p_a \left[1 + \left(\frac{z}{r_C}\right)^2\right]^{-3\beta_{atm}/2} , \tag{28}$$

where p_a is the ambient medium pressure at the center of the host galaxy, r_C is the galaxy atmosphere core radius and $\beta_{atm} = 0.73$. We simulate this profile for two different core radii and a comparison of these is plotted in Fig. 8. We see that the profile with the smallest core radius has a very steep slope meaning that the jet will notice the low pressure outside earlier and therefore expand more than a jet with the other profile. For instance, Figs. 11 and 12 show jets with a decaying ambient medium pressure profile with core radius of $r_C = 20$ pc and $r_C = 50$ pc, respectively. It can readily be seen that the jet in the galaxy with a smaller core radius expands more than the jet in a bigger one over the same distances, where the former expands about five times its initial radius and the latter about three times its initial radius.

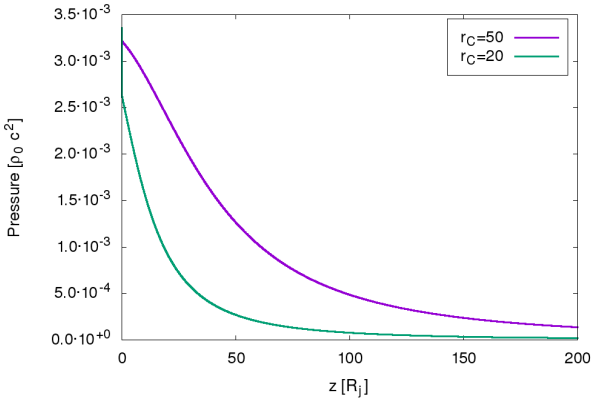

Figure 8: Pressure profiles comparisons.

We now focus on the effects that the jet expansion has over its parameters. First of all, if we direct our attention to the density panel of either model (Jp22 or Jp52), we see that the density of the jet decreases as the jet expands. Then the pressure inside the jet also decreases to the point where the jet and the ambient medium are in equilibrium of pressures, this is the main reason for the jet expansion. Moving on, a fundamental principle in fluid dynamics is revealed, Bernoulli's principle, which states that an increase in the speed of the fluid occurs with a decrease of the fluid pressure in hot jets, for instance, the Lorentz factor increases as the jet expands and reduces its internal pressure. The plot in Fig. 9 manifests this specific principle, as the jet expands the flow gets accelerated and the bigger the expansion the higher is the acceleration. We now analyse the effect of the magnetic field on the jet expansion and hence its acceleration. Figure 9a shows that the jet expansion depends on its magnetization (where the radius of the jet corresponds to the distance to the point where the traces is 0.5), this is caused by the effect of magnetic tension. When the magnetic field is larger it exerts a stronger force opposing the expansion of the jet. Then these different expansions of jets cause different accelerations, in fact, Fig. 9b agrees with that, where more expanded jets present higher accelerations.

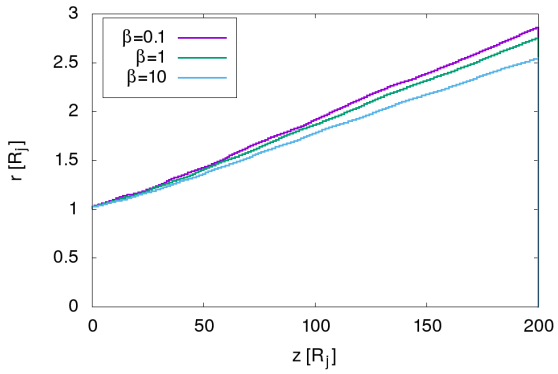

(a) Different jet expansions for different magnetizations in the series of models Jp5X.

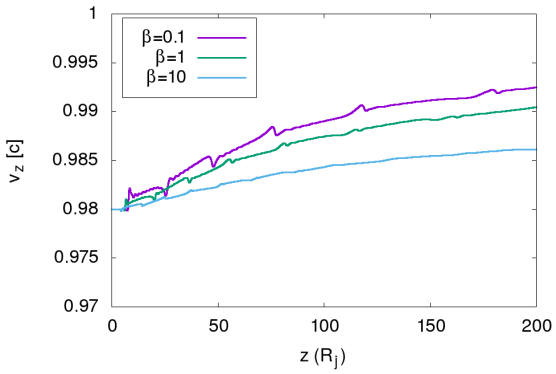

(b) Different accelerations caused by different expansions of the jets (and hence different magnetizations) in the series of models Jp5X.

Figure 9: Plots showing the effect of the magnetic field, through magnetic tension, on different jet properties.

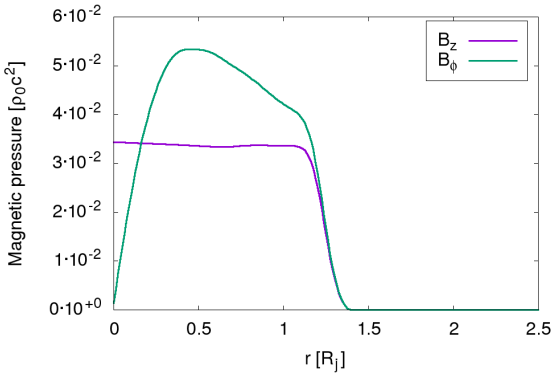

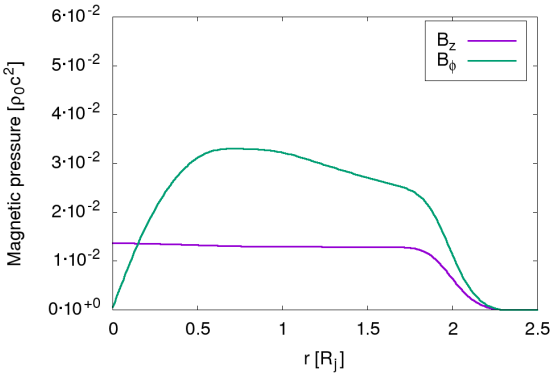

Figure 10: Magnetic field components at $z = 50$ pc and $z = 150$ pc in the model Jp52.

Finally, the flux freezing effect, which we commented in the introduction, is clearly manifested here: the poloidal magnetic field significantly decreases with respect to the toroidal magnetic field component as the jet expands. In Fig. 10 we plot two radial profiles of these magnetic field components for the Jp52 model at different z showing the steeper decrease of the poloidal component as well as the overall decrease due to flux freezing too.

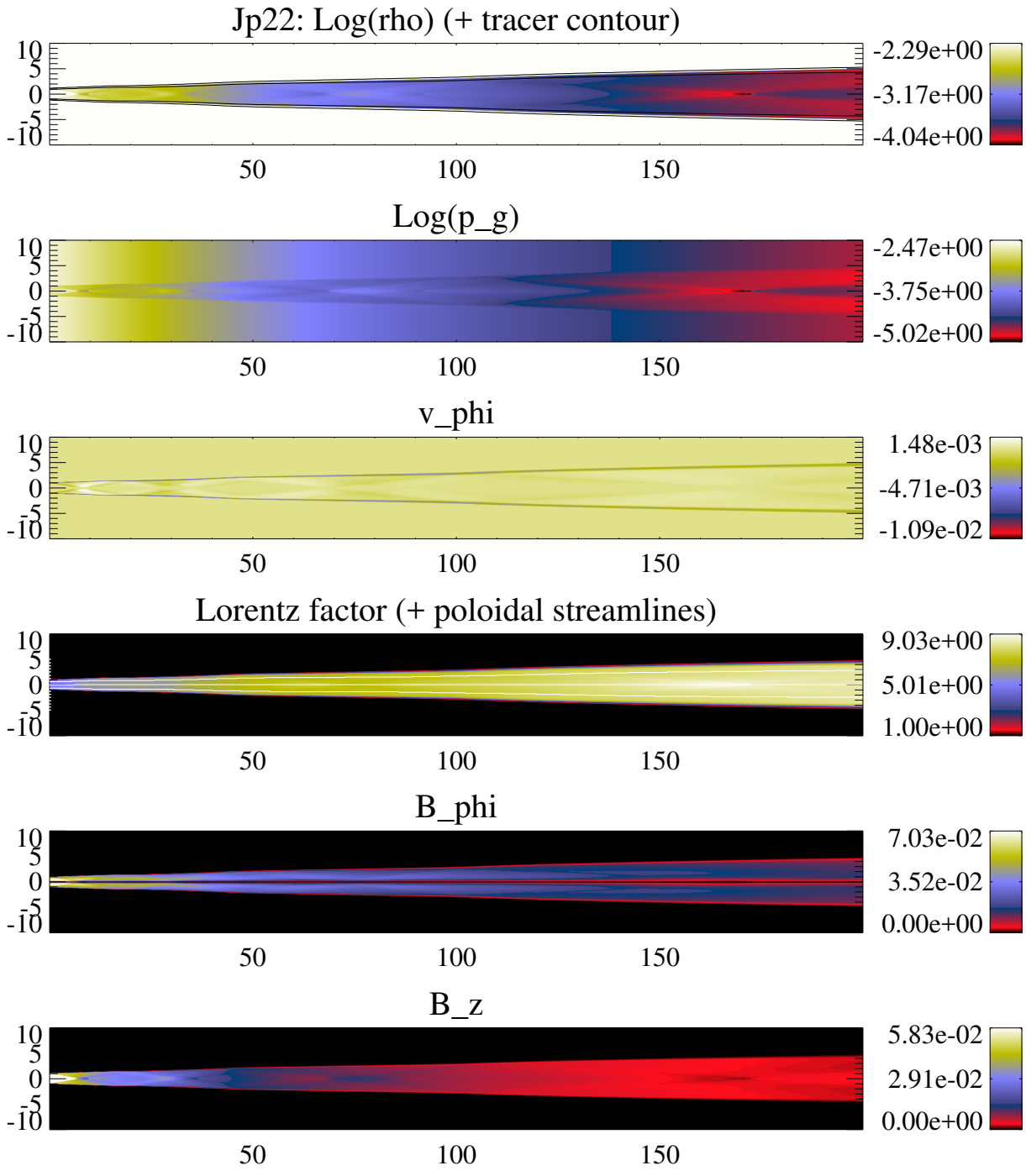

Figure 11: Model of a jet with $\beta = 1$ with an overpressure parameter $K = 1$ in a galaxy with core radius $r_C = 20$ pc.

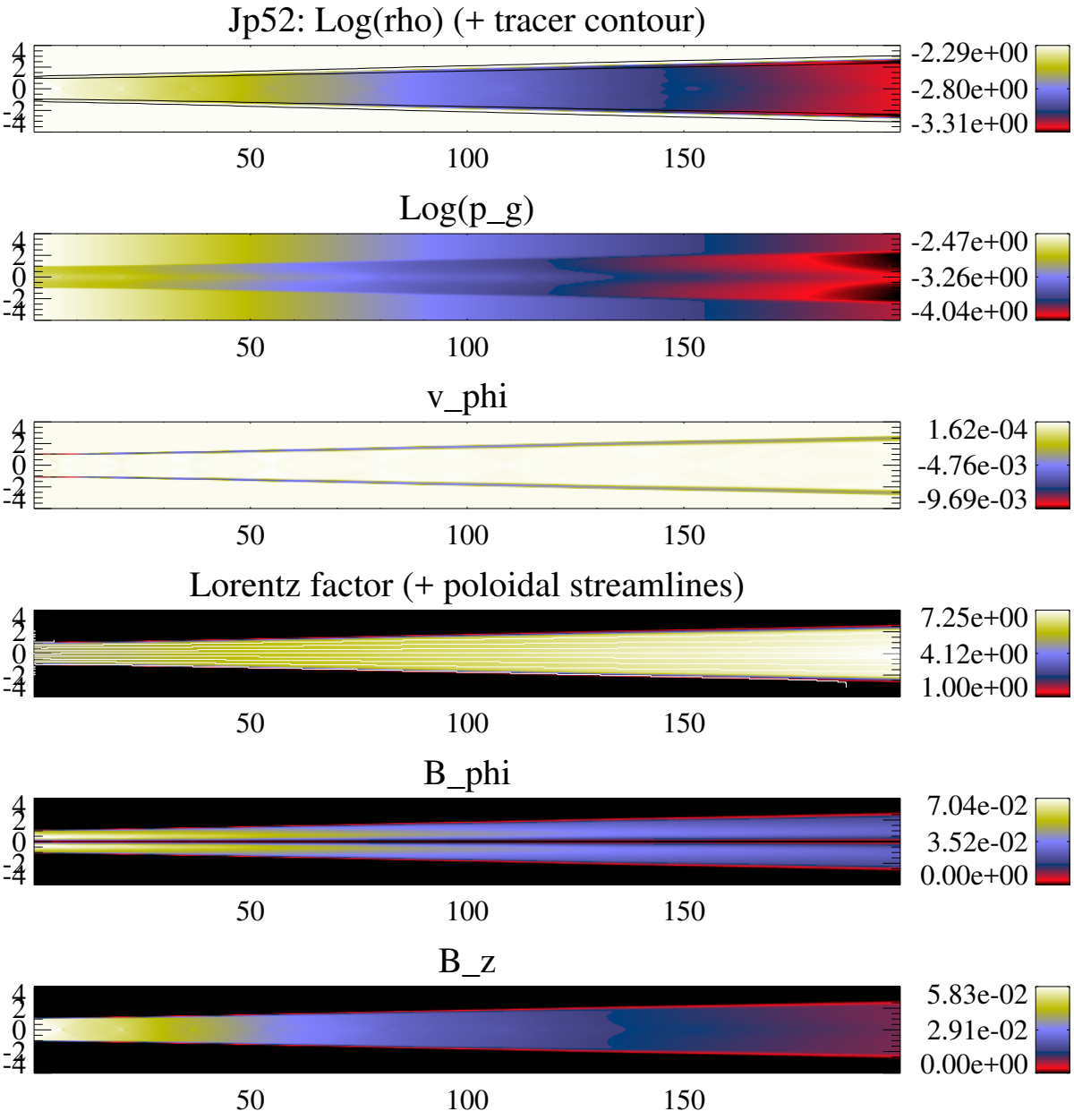

Figure 12: Model of a jet with $\beta = 1$ with an overpressure parameter $K = 1$ in a galaxy with core radius $r_C = 50$ pc. Note the change in the radial scale with respect to Fig. 11.

4.3 Deceleration by mass entrainment

We finally proceed to present jet models with deceleration caused by mass entrainment. In this case we have executed longer simulations up to 2 kpc because it takes some time for the jet to be decelerated and, as expected from observations, the deceleration of jets takes place at scales of the order of the kpc [9]. Figures 13 and 14 show two jets for different mass loads, corresponding to the model Jm12 and Jm22. On the one hand, the first one hardly feels the mass load as, if we check the Lorentz factor, the jet still gets accelerated because of the jet expansion. We have changed the toroidal velocity panel for a panel for the tracer because we have already checked that the approximations taken into account are correct and does not add any additional information. We see that the tracer has a small apperture with respect to other panels but the larger values of it are still around the axis. On the other hand, the Jm22 jet has been affected by the mass load, if we focus on the tracer we see that it has expanded more and it has also got more diluted as material from the ambient medium, which we programmed to have tracer 0, has became part of the jet.

To have a clearer idea on how mass loading affects the properties of the jet we plot the tracer, the axial velocity, the internal energy, the density, the jet radius and the magnetizations evolution along the axial coordinate in Fig. 15. The plot with the tracer (Fig. 15a) clearly shows which model is more affected by the mass entrainment. It hardly affects models Jm02 and Jm12, whereas model Jm22 is very mixed with the stellar wind and Jm30 is a fiducial model where there is no load from the ambient medium and the tracer has constant value 1. Moving on to Fig. 15b we see that the Jm22 model gets significantly decelerated with respect to the others. In these simulations there is a constant tension between the acceleration produced by the jet expansion and the opposite effect created by the mass loading. In these figures we see that the Jm12 model is slightly affected by mass entrainment, but does not show all features characteristic of mass loading a jet. Figure 15c shows that internal energy decreases, as the jet expands, due to its cooling, but model Jm22 shows a moderate reduction in internal energy caused by the dissipation of kinetic energy, which is transformed into internal energy. We now focus on how the radius of the jet evolves. On the one hand, one should think that as the jet gets load its radius would increase due to the increase in pressure. On the other hand, the jet gets decelerated with the decrease of the Lorentz factor. When the Lorentz factor decreases, the contribution to the magnetic tension increases as it scales $\propto \Gamma^{-2}$. Looking at Fig. 15d we see two phases on the evolution of the radius of the model Jm22: (i) the jet does not get expanded as much as the others, where the magnetic tension is sufficiently important to reduce the expansion and (ii) at longer distances the magnetic field has dropped enough to let the jet expand and it even surpases the other jets radii. With respect to the density, models Jm30, Jm02 and Jm12, which are hardly or not affected by mass entrainment, present the same densities over the axial distance. Figure 15e shows that the density in the model Jm22 is incresead, with respect to the other, because of the mass load and tends to the same value of the other models when the jet expands. We finally check that the average magnetization of the jet with mass load (Fig. 15f) is more reduced than the others due to the addition of unmagnetized particles to it.

All these results have been drawn for models with magnetization $\beta = 1$, we cannot obtain conclusive results of the effect of the magnetization on the mass entrainment of jets because, for our fixed parameters, the jet radius increases with magnetization. Even though the power of the jet is the same for either magnetization, the power per unit area is lower for models with bigger radii and hence being more affected by the mass

entrainment. To do that study we would need to move onto another space of parameters where the radii of the jets would be fixed. We have also checked that if we increase the mass entrainment rate by another order of magnitude jets get completely disrupted.

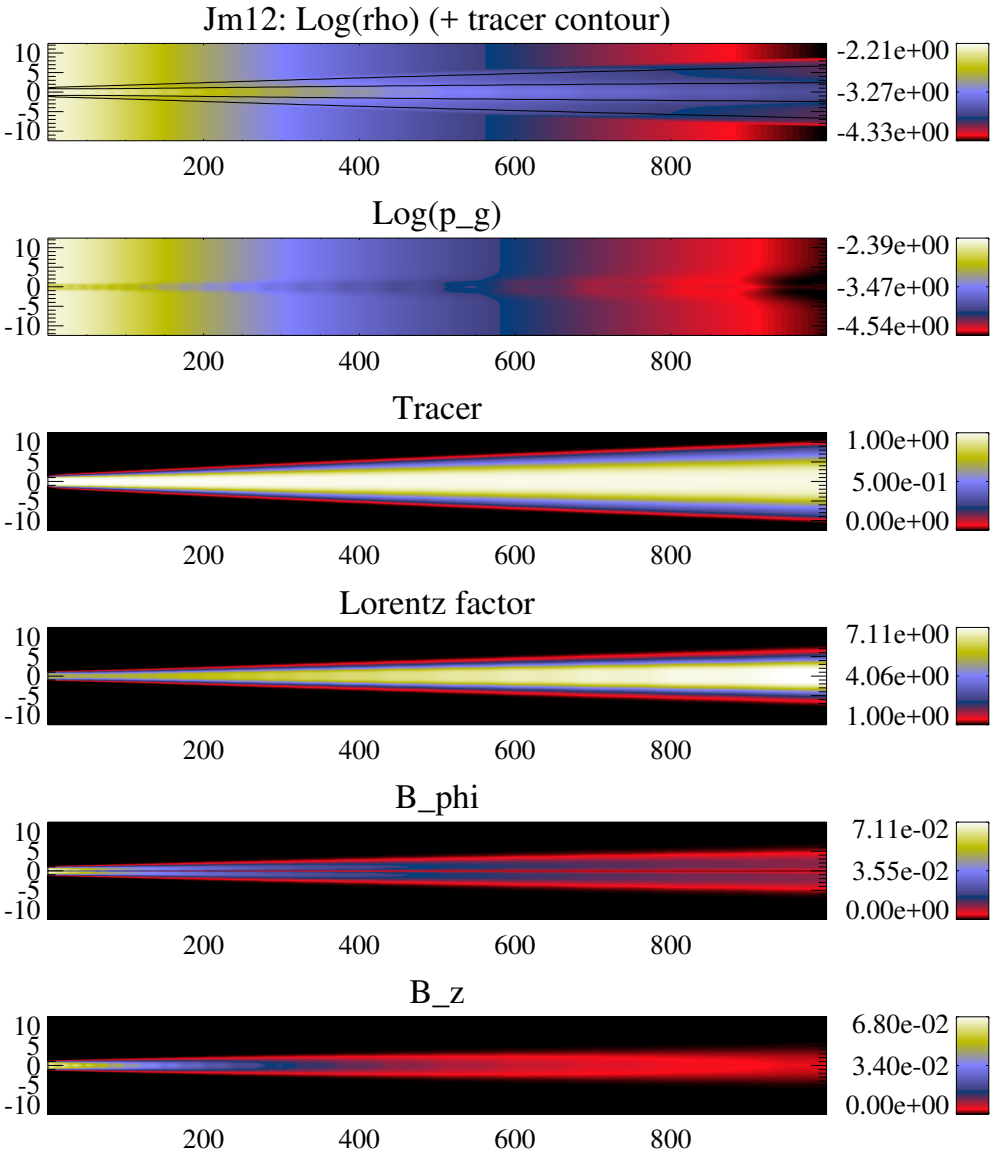

Figure 13: Jet model Jm12 with $\beta = 1$, an overpressure parameter $K = 1$ and in a galaxy with core radius $r_C = 250$ pc. The tracer contour lines in the first panel correspond to values of the tracer of 0.5 (this line corresponds to the radius of the jet) and 0.95.

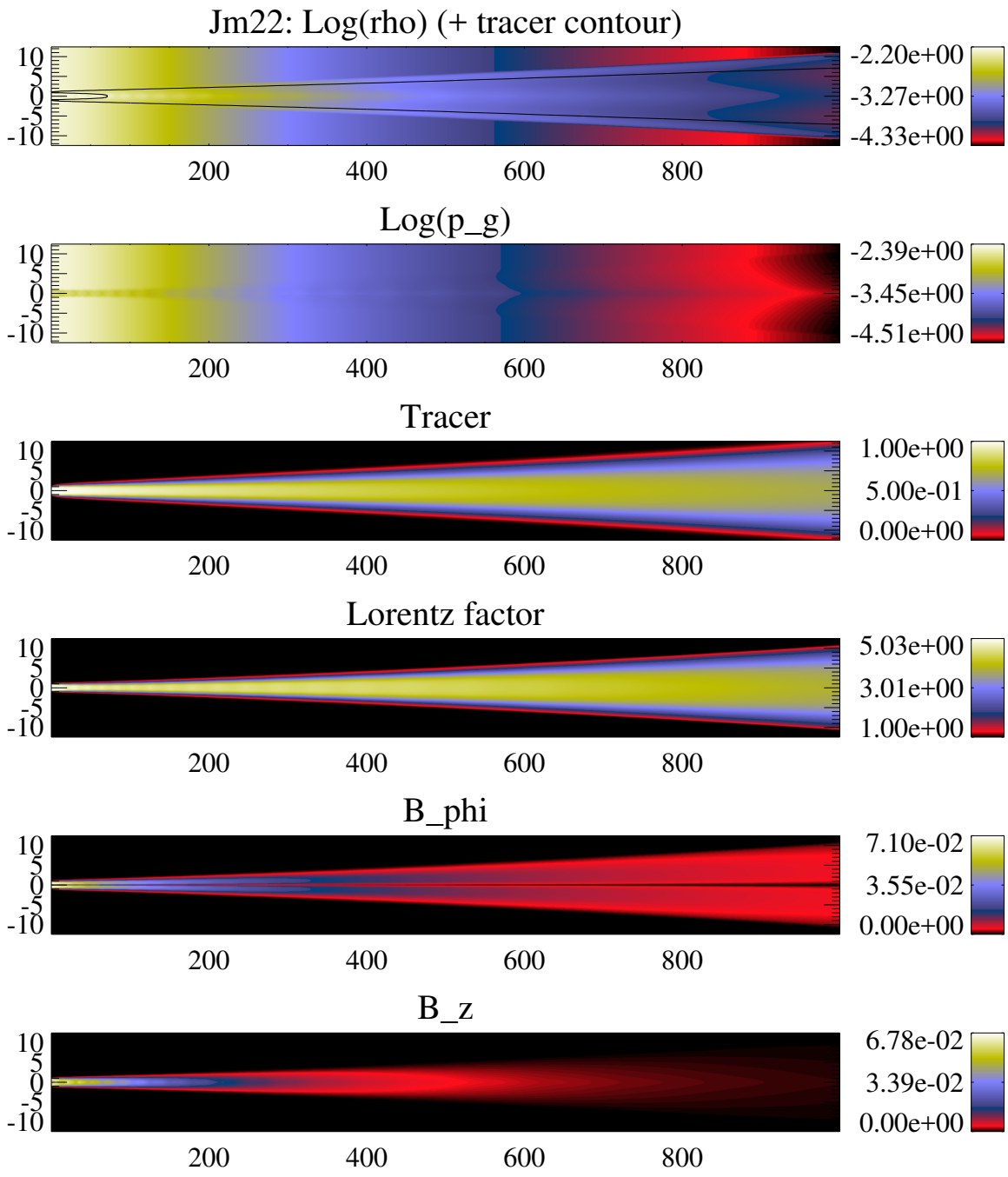

Figure 14: Jet model Jm22 with $\beta = 1$, an overpressure parameter $K = 1$ in a galaxy with core radius $r_C = 250$ pc and the biggest mass entrainment rate among our models.

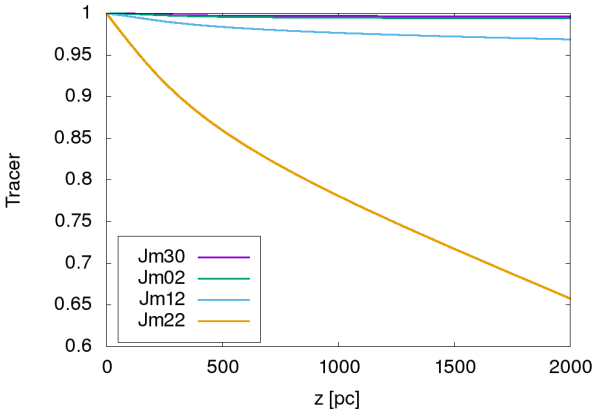

(a) Tracer at the center of the jet.

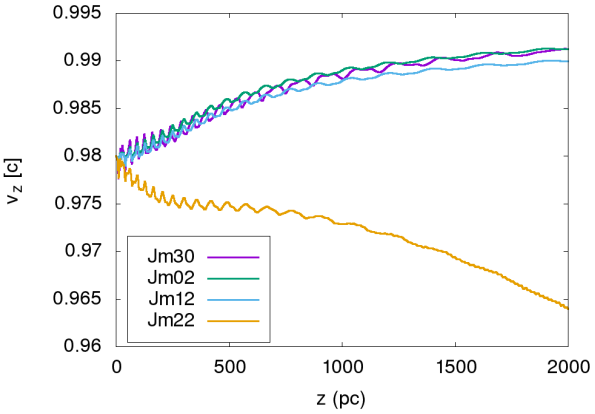

(b) Axial velocity at jet's center.

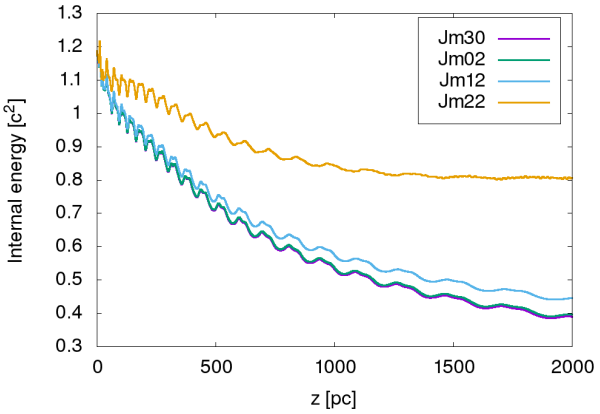

(c) Averaged internal energy.

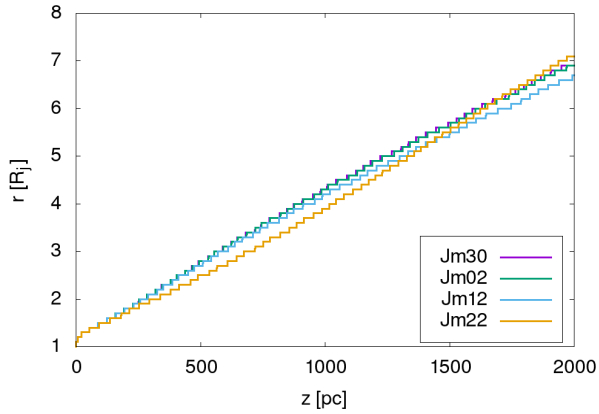

(d) Radius of the jet.

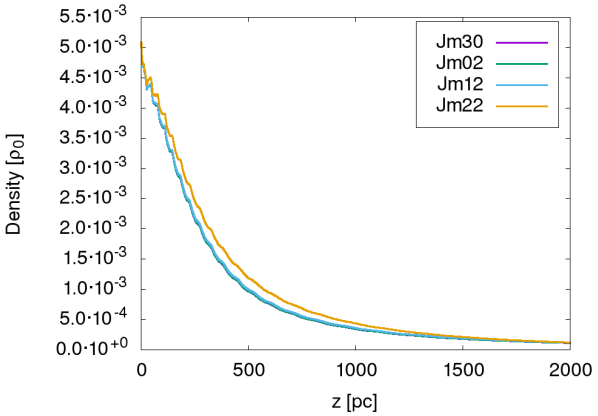

(e) Averaged density.

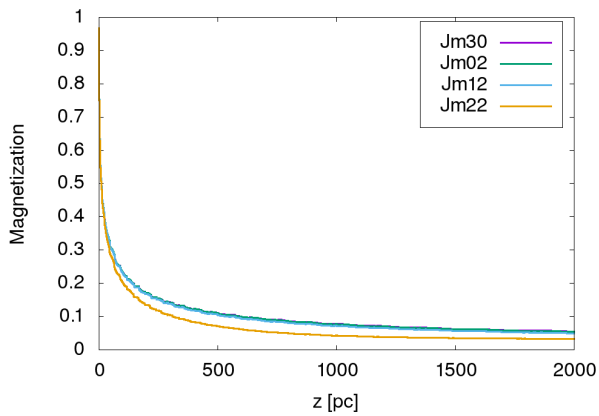

(f) Averaged magnetization.

Figure 15: Different parameter along the axial coordinate for models Jm30, Jm02, Jm12 and Jm22.

5 Summary and conclusions

We presented the astrophysical context of extragalactic jets and gave a qualitative description on their formation. We focused on the study of steady state, axisymmetric jets and introduced the equations and approximations to model them. We gave a description of the numerical methods used to simulate the model. We have simulated a battery of jet models with different ambient mediums and studied their effect on the properties of the jet, on which we base the following conclusions.

1. Jets propagating through pressure-decreasing atmospheres expand and cool. At the same time, as a consequence of Bernoulli's principle, the flow in the jet accelerates.

2. The expansion rate depends on the jet magnetization, the more magnetized jets expand slower as a result of the action of the magnetic tension.

3. Along the jet expansion, both poloidal and toroidal components of the magnetic field decrease as expected from the condition of magnetic flux freezing making the toroidal field dominate at large distances.

4. The flow acceleration caused by Bernoulli's law can be counterbalanced with mass entrainment, for large enough entrainment rates, causing the deceleration of the flow and the eventual disruption of the jets at large enough distances.

5. An interesting interplay has been found between the process of mass entrainment (which tend to decollimate and decelerate the jet), and the jet magnetization (that tries to keep it collimated under the action of the magnetic tension) which deserves further analysis.

6 Resum i conclusions

Hem presentat el context astrofísic dels jets extragalàctics i hem donat una descripció qualitativa del seu procés de formació. Ens hem centrat en l'estudi de jets estacionaris i amb simetria axial i introduït les equacions i aproximacions per a modelitzar-los. També hem donat una descripció dels mètodes numèrics usats per a simular el model. Hem simulat una bateria de diferents models de dolls amb diferents condicions d'ambient i estudiat el seu efecte sobre les propietats dels mateixos, sobre les quals basem les següents conclusions.

1. El jets que es propaguen a traves d'atmòsferes amb pressió decreixent s'expandeixen i es refreden. Alhora, com a conseqüència del principi de Bernoulli, la corrent del jet s'accelera.

2. El ritme d'expansió depén de la magnetització del jet, els jets més magnetitzats s'expandeixen més lentament com a resultat de l'acció de la tensió magnetica.

3. Durant l'expansió del jet, tant la component poloidal com la toroidal del camp magnetic decreixen degut a la condició de congelament del flux magnetic, fent que la component toroidal del camp domine a major distàncies.

4. L'acceleració del jet a causa del principi de Bernoulli competeix amb el carregament de massa que, per a ritmes de càrrega de massa sufiecientment grans, desaccelera el jet i, fins i tot, desfent-lo a distancies suficientment grans.

5. S'ha trobat una interesant interacció entre el proces de càrrega de massa (que tendeix a desaccelerar i decolimar el jet) i la magnetització del jet (que intenta mantindre el doll colimat baix l'acció de la tensió magnètica), cosa que mereix un estudi en més profunditat.

References

[1] B. L. Fanaroff and J. M. Riley. The morphology of extragalactic radio sources of high and low luminosity. *Monthly Notices of the Royal Astronomical Society*, 167(1):31P, 1974.

[2] M. Boettcher, D. E. Harris, and H. Krawczynski. *Relativistic Jets from Active Galactic Nuclei*. Wiley-Vch, 2012.

[3] S. S. Komissarov, O. Porth, and M. Lyutikov. Stationary Relativistic Jets. *Computational Astrophysics and Cosmology*, 2015.

[4] José María Martí and Ewald Müller. Grid-based methods in relativistic hydrodynamics and magnetohydrodynamics. *Living Reviews in Computational Astrophysics*, 1(1):3, Dec 2015.

[5] M. Perucho, J. M. Martí, R. A. Laing, and P. E. Hardee. On the deceleration of Fanaroff–Riley Class I jets: mass loading by stellar winds. *Monthly Notices of the Royal Astronomical Society*, 441(2):1488, 2014.

[6] M. Bowman, J. P. Leahy, and S. S. Komissarov. The deceleration of relativistic jets by entrainment. *Monthly Notices of the Royal Astronomical Society*, 279(3):899, 1996.

[7] G. Ghisellini and A. Celotti. The dividing line between FR I and FR II radio-galaxies. *A&A*, 379(1):L1–L4, 2001.

[8] M. J. Hardcastle, D. M. Worrall, M. Birkinshaw, R. A. Laing, and A. H. Bridle. A chandra observation of the x-ray environment and jet of 3c 31. *Monthly Notices of the Royal Astronomical Society*, 334(1):182, 2002.

[9] R. A. Laing and A. H. Bridle. Systematic properties of decelerating relativistic jets in low-luminosity radio galaxies. *Mon. Not. Roy. Astron. Soc.*, 437(4):3405–3441, 2014.